

## Graphical Abstract

### Nucleation and Growth of Stellated Gold Clusters: Experimental Synthesis and Molecular Dynamics Study

*J. M. Cabrera-Trujillo, J.M. Montejano-Carrizales, J.L. Rodríguez-López*

*W. Zhang, J.J. Velázquez-Salazar, and M. José-Yacamán*

# Nucleation and Growth of Stellated Gold Clusters: Experimental Synthesis and Molecular Dynamics Study

J. M. Cabrera-Trujillo\*

*Facultad de Ciencias, Universidad Autónoma de  
San Luis Potosí, 78000 San Luis Potosí, Mexico*

J. M. Montejano-Carrizales

*Instituto de Física, Universidad Autónoma de  
San Luis Potosí, 78000 San Luis Potosí, Mexico*

J. L. Rodríguez-López†

*Instituto Potosino de Investigación Científica Y Tecnológica, A.C.  
División de Materiales Avanzados; 78216 San Luis Potosí, Mexico*

W. Zhang, J.J. Velázquez-Salazar, and M. José-Yacamán

*Department of Physics and Astronomy,*

*University of Texas at San Antonio one UTSA Circle, San Antonio TX 78249 USA*

(Dated: July 26, 2010)

## Abstract

An experimental and theoretical study on the structure and energetics of stellated gold clusters at several sizes is presented. Systematic molecular dynamics simulations on Kepler-Poisont classified clusters are performed based on cubo-octahedral and icosahedral cores, following present and previous studies that suggest stellated clusters grew up from these seeds. For cluster sizes up to 10802 atoms full atomistic molecular dynamics simulations at room temperature have been carried out. Results show that stellated clusters in the bigger size regime maintain their star-like shape at room temperature, and by means of linear fitting of energy data to proper function models, it is predicted that the two type of stellated structures might coexist at room temperature for relatively large sizes, being these findings in good agreement with experimental results.

PACS numbers: \*

## I. INTRODUCTION

The present study on stellated gold nanoparticles (NPs) is driven mainly by fundamental and applied *leit motivs*. From the fundamental point of view, we pursue the hypothesis that stellation on clusters (Kepler-Poisont solids) is a process that follows after the nucleation of well defined structures, such as octahedra and icosahedra (platonic shapes) and cuboctahedra and truncated octahedra (archimedean solids)<sup>1</sup>, supported the idea by the *seed growth approach* in many different syntheses of anysotropic noble metal NPs<sup>2-7</sup>; where each one of these shape classifications could be located in size regions—although with not well defined boundaries—of the cluster growth.

From the applied point of view, in the nanoparticle research fields there are now well established facts that drive applications researchs in these fields, *i.e.*, the properties of the systems are influenced by the NPs size, but also is known now that the shape strongly influences the physical and chemical properties of the NPs<sup>8-10</sup>. Thus, in the problem of understanding how shape and size of metallic NPs relate each other, and how these factors influence the properties of the systems under study, becomes more complex but certainly, more fascinating too. Because of the facile synthesis, their enhanced absorption and scattering cross sections that Au and Ag NPs show under electromagnetic radiation, and because of their potential nontoxicity, noncitotoxicity, and their good biocompatibility, they are widely studied for biological imaging and biomedicine applications (cancer cell imaging and destruction, photothermal therapy, among others)<sup>11-13</sup>. In particular, Au NPs generate heat under proper electromagnetic radiation, being this heating effect strong when the energy of the incident radiation is close to the plasmon frequency of the metallic NPs<sup>14</sup>.

Among factors that had contributed to the comprehension, understanding and development of the energetics, thermodynamics, and kinetics of atomic and molecular clusters<sup>15</sup>, we can mention the interplay between spectroscopy<sup>2</sup>, and theoretical techniques based on solid-state physics (SSP)<sup>16-19</sup> or other potentials supported by the density-functional theory (DFT)<sup>20,21</sup>. The development of geometric models based on platonic solids<sup>22</sup>, or on the most probably structures in experiments generated by quenching technique in a molecular dynamics simulation<sup>23</sup> or by genetic algorithms<sup>24</sup> provide us with suitable geometrical and inter-atomic potential models are available to study small and large number of particles assemblies through non-quantum methodologies like Monte Carlo or molecular dynamics

simulations (MDS) at high confident levels.

Under this theoretical framework, extensive studies on metallic clusters have been carried out<sup>15</sup>. For instance, by using the excess-energy per number of surface atoms on clusters as a diagnostic tool, Balletto *et al.*<sup>25</sup> had found and explained why gold clusters prefer fcc structures at sizes larger than 600 atoms, and strong competitions between  $D_h$  and fcc near  $N = 400$  atoms. Two potential models based on DFT and SSP theories were used in those calculations, and they also found agreement with other results obtained at different levels of calculation.

Several potential models for transition and noble metals, based on the tight-binding second-moment approximation (TBSMA)<sup>16,17</sup>, have been proposed. For instance, the parameterization of Rosato *et al.*<sup>18</sup> (RGL model) and a second parameterization of the RGL due to Cleri and Rosato<sup>19</sup> (CR), among others<sup>25,26</sup>. All these kind of models include the repulsive pairwise Born-Mayer potential to stabilize the system. One of the main characteristics of those models is the inclusion of many body effects ensuring correct estimation of several bulk properties, like cohesive energies, vacancies, surface effects, etc. The correct estimation of those bulk properties, mainly cohesive energy, surface effects, and surface reconstructions, has given confidence to extend the model to atoms in a cluster environment<sup>15</sup>. Thus, with these reliable potential models at hand, general trends can be obtained. For example, significative knowledge on the thermal behavior of gold clusters is well known for specific geometries based on crystalline and non-crystalline motifs, like fcc, icosahedral and decahedral clusters<sup>15</sup>.

In this work, by means of classical MD simulations, and the CR interatomic potential model, we study the structure and dynamics of stellated gold nanoclusters with icosahedral and cuboctahedral seeds, biased mainly by the present experimental results on gold nanoparticles and previous reports on stellated (piñata like) clusters<sup>2</sup>. Stellated Au nanoparticles have been synthesized at room conditions of temperature and pressure. Figure 1 shows the great rate of production of these stellated clusters, and the high-resolution transmission electron microscopy (HRTEM) images at different orientations clearly show highly symmetric pyramidal structures with slightly smoothed apices. From experimental facts, it has been observed high stability in the clusters shapes, *i.e.*, they do not change in days and even months after depositing them in an inert environment. These facts induced the hypothesis that stellated gold particles could have cuboctahedral and icosahedral cores, but both with

a surface tetrahedral pyramidal growing along the high symmetry axes. In order to give some insight into the structural and thermal behavior of these stellated structures, mainly at room temperature, we present a systematic study of the structural and thermal behavior of two groups of gold clusters whose construction was based on those structures.

## II. EXPERIMENTAL DETAILS

### A. Materials and Methods

Hydrogen tetrachloroaurate trihydrate ( $\text{HAuCl}_4 \cdot 3\text{H}_2\text{O}$ ), Silver nitrate, trisodium citrate dehydrate, ascorbic acid were purchased from Sigma-Aldrich and used as received. Multi-branched polyhedral gold nanoparticles were prepared by colloidal reduction in aqueous solution at ambient conditions according to previous literature methods<sup>2</sup>. A volume of 0.5 mL of 0.1 M  $\text{HAuCl}_4$  aqueous solution (50  $\mu\text{mol}$ ) was rapidly added into an aqueous solution of ascorbic acid (2 mmol in 40 mL  $\text{H}_2\text{O}$ ) under vigorous stirring. The solution immediately changed its color to opaque orange-red within  $1 \approx 2$  seconds. All the samples were purified by washing with ethanol and centrifuging, and finally dispersed in ethanol.

### B. TEM Characterization

The Au nanostar samples were characterized by ultra-high resolution scanning electron microscope (SEM) FEG Hitachi S-5500 (0.4 nm at 30 kV) with BF/DF Duo-STEM detector and high resolution transmission electron microscope (HRTEM) Jeol JEM-2010F FE-TEM with an accelerating voltage of 200 kV, equipped with a Schottky-type field emission gun and a point-to-point resolution of 0.19 nm. Samples for TEM studies were prepared by placing directly the gold nanoparticles onto a holey carbon TEM grid.

## III. THEORETICAL BACKGROUND AND METHODOLOGY

The functional form of the TBSMA for pure atomic systems, also known as Gupta potential<sup>16</sup>, is given by

$$V(r_i) = \sum_{j \neq i} A \exp(-p \Delta r_{ij}) - \left( \sum_{j \neq i} \xi^2 \exp(-2q \Delta r_{ij}) \right)^{1/2}. \quad (1)$$

The first term is the repulsive Born-Mayer pairwise potential, and the second one is the tight-binding based attractive non-pairwise potential which takes into account many-body effects.  $\Delta r_{ij} = (r_{ij} - r_0)/r_0$  is the fractional change in distance between atom  $i$  and atom  $j$ , and  $r_0$  is the distance between first nearest-neighbors in bulk. The five parameters,  $A, \xi, p, q$ , and  $r_0$  must be determined for each particular transition or noble metal atom by a parametrization procedure using bulk data<sup>18,19,27</sup>. If only first nearest-neighbors are taking into account in Eq. (1), and if the equilibrium condition is fulfilled, then the number of parameters is decreasing from five to three<sup>17</sup>:

$$A = \frac{q}{p-q} \frac{|E_{\text{coh}}|}{Z}, \quad (2a)$$

$$\xi = \frac{p}{p-q} \frac{|E_{\text{coh}}|}{\sqrt{Z}}, \quad (2b)$$

where  $E_{\text{coh}}$  is the experimental cohesive energy of bulk used in the parameterization, and  $Z$  is the number of first nearest-neighbors in the crystal.

Some sets of parameters for gold (fcc crystal) are given in Table I. In these models values for  $A$  and  $\xi$  are very close to those calculated from Eqs. (2) using the experimental value  $E_{\text{coh}} = -3.78$  eV/atom and  $Z = 12$ , both from gold fcc-crystal<sup>28</sup>. At a first sight, differences and similarities between these potential models can be obtained from the fractional change in total energy accompanying a fractional change in distance between first nearest-neighbors  $\epsilon = (r_{ij} - r_0)/r_0$ , which at second order approximation in  $\epsilon$  is roughly given by

$$\frac{\Delta E}{|E(0)|} \approx \sigma_1 \epsilon^2, \quad (3)$$

where  $\Delta E = E(\epsilon) - E(0)$ ,  $E$  is the total energy, and  $\sigma_1 = pq/2$ , see Ref. 25. The  $\sigma_1$  values for the CR and RGL models differ 1.5% each other, and the values among BFFMM and CP differ 0.8%; corresponding the lower and bigger values to the CR and CP models, respectively. Thus, according to  $\sigma_1$  values and Eq. (3), the BFFMM potential is as sticky as the CP model, and the CR model is slightly less sticky than the RGL, being CP more sticky than the CR model. However, according to the formula

$$\frac{\Delta E}{|E(0)|} = \frac{1}{p-q} (q(e^{-p\epsilon} - 1) - p(e^{-q\epsilon} - 1)), \quad (4)$$

where no approximations in  $\epsilon$  have been used, the similarity between the BFFMM and CP models only occurs for displacements less than 1.5% of  $r_0$ , as can be seen from the plots in Fig. 3. In fact, crossovers between the CP and the BFFMM, RGL and CR models occur at

TABLE I: Comparision of published potential parameters for gold derived by fitting bulk experimental data to values calculated using the Gupta functional form given by Eq. (1). We note that values for the lattice constant and cohesive energy, ( $\sqrt{2} r_0$ ,  $E_{coh}$ ), in each model are experimental values taken from Kittel<sup>28</sup>, but on different potential versions: the parameterization of Rosato *et al.*<sup>18</sup> (RGL model, Kittel 1972); the second parameterization of the RGL due to Cleri and Rosato<sup>19</sup> (CR, Kittel 1966); whereas Balleto *et al.*<sup>25</sup> (BFFMM) and Chamati and Papanicolaou<sup>26</sup> (CP) use parameters from Kittel, 1996. For the CP model we have used the calculated values<sup>26</sup> shown in the row.

Model <sup>a</sup>	$p$	$q$	$\xi$ (eV)	$A$ (eV)	$\sqrt{2} r_0$ (Å)	$-E_{coh}$ (eV/atom)
RGL <sup>18</sup>	10.15	4.13	1.8398 <sup>b</sup>	0.2161 <sup>b</sup>	4.08	3.78
CR <sup>19</sup>	10.229	4.036	1.790	0.2061	4.079	3.779
BFFMM <sup>25</sup>	10.53	4.30	1.855	0.2197	4.07	3.78
CP <sup>26</sup>	14.6027	3.12572	1.32795	0.08170	4.068	3.76

<sup>a</sup>Model's name is proposed from the initials of the author and coauthors of the cited article.

<sup>b</sup>Values obtained using Eqs. (2).

$\epsilon \simeq 0.0085$ ,  $\epsilon \simeq 0.093$ , and  $\epsilon \simeq 0.115$  respectively. Thus, according to Eq. (4) the CP model is less sticky than the other potentials, but for  $\epsilon \gtrsim 0.115$ .

### A. Simulation Details

In order to perform MD simulations at room temperature of the SC and SI gold clusters described above, the Au potential model given by Eq. (1) was used, applying the four parameter sets given in Table I under the GROMOS96 scheme<sup>29</sup>. This package applies the leap-frog algorithm to integrate the Newton's classical equations of motion under vacuum or periodic boundary conditions<sup>30</sup>. High numerical stability is ensured for a time-step of 2 fs, if shake method is applied; otherwise 0.5 fs. Those time-steps values are commonly used for flexible biological molecules<sup>29</sup>; for metallic atoms a practical value for the time-step is 1 fs<sup>31</sup>. Also under this scheme, the system could be weakly or strongly coupled to a temperature bath using the Berendsen's thermostat<sup>32</sup>. The numerical ensemble produced by MDS applications using Berendsen's thermostat is the weak-ensemble<sup>33</sup>, which has intermediate

property between the canonical  $(N, V, T; \alpha = 0)$  and microcanonical  $(N, V, E; \alpha = 1)$  ensembles. Here,  $\alpha$  is a constant in equilibrium but dependent on the temperature coupling parameter<sup>32,33</sup>. In the practice,  $\alpha$  is determined from the ratio of standard deviations of kinetic and potential energies,

$$\alpha = \sqrt{\langle (\delta E_{\text{Kin}})^2 \rangle / \langle (\delta E_{\text{Pot}})^2 \rangle}, \quad (5)$$

where  $\delta E_z(t) = E_z(t) - \langle E_z \rangle$  stands for the instantaneous fluctuation of property  $z$  (kinetic or potential energy), and  $\langle \rangle$  denotes average time.

## B. Geometrical Description

Since any stellated gold clusters considered in this work are made up of one icosahedral or one cuboctahedral cluster in the core, and regular tetrahedral clusters attached to their (111) faces, we will refer them as stellated icosahedral (SI) and stellated cuboctahedral (SC) clusters, respectively. Specifically, each SI gold cluster is made up of one Mackay icosahedral cluster with  $(n = k + 1, k \geq 1)$  shells and  $N(n) = \frac{10}{3}n^3 - 5n^2 + \frac{11}{3}n - 1$  atoms, and twenty tetrahedral clusters, each with  $N_{\text{Td}}(k) = \frac{k(k+1)(k+2)}{6}$  atoms and attached to each one of the twenty (111) facets of the icosahedral cluster. In a similar way, each SC gold cluster is made up of one cuboctahedral cluster with  $N(k+1)$  atoms, and eight tetrahedral clusters, each with  $N_{\text{Td}}(k)$  atoms and attached to each one of the eight (111) facets of the cuboctahedral cluster. Hence, the number of atoms of any  $\text{SI}_k$  cluster is given by  $N_{\text{SI}}(k) = N(k + 1) + 20N_{\text{Td}}(k)$ , while  $N_{\text{SC}}(k) = N(k + 1) + 8N_{\text{Td}}(k)$  is the number of atoms of any  $\text{SC}_k$  cluster.  $N_{\text{SI}}(k)$  and  $N_{\text{SC}}(k)$  are only different in the number of tetrahedrons, and they can also be expressed as

$$N_{\text{SC}}(k) = \frac{14}{3}k^3 + 9k^2 + \frac{19}{3}k + 1, \quad (6a)$$

$$N_{\text{SI}}(k) = \frac{20}{3}k^3 + 15k^2 + \frac{31}{3}k + 1, \quad (6b)$$

with  $k \geq 1$ .

The gold clusters considered in this work are those SC clusters with  $k \leq 13$ , and those SI with  $k \leq 11$ , shown in Fig. 4. In all the initial geometrical models the distance between first nearest-neighbor atoms is fixed to the first nearest-neighbor distance of bulk gold,  $r_0 = 2.88 \text{ \AA}$ .

## IV. RESULTS AND DISCUSSION

Figure 4 displays the unrelaxed stellated clusters used in this study. To prepare these SI and SC gold clusters for MD simulations at  $T = 298$  K, we have first slightly relaxed each one of them with the steepest-descents method using the four potential models in Table I. Although the main purpose of the minimization procedure is to reduce the internal strain of the cluster, and the consequently reduction of computer effort at the equilibration period, we have analyzed these results to gain insight investigating how the residual stress is reflected into the structures, how the surface and volume contributions to the total energy behaves as function of cluster size, and what type of the stellated structures is the most favorable. Similarities and differences between the results obtained using older and newer gold potential models (Table I), are also enhanced and analyzed at this stage in order to choose the appropriate potential to perform the simulations at room temperature. Thus, a conscientious analysis of the structural and energetic results obtained under this procedure is presented in Sec. IV A. In Sec. IV B, we have posed similar questions for the equilibrated clusters at  $T = 298$  K, and the results have been analyzed in the same way, but only for the CR potential model, which was elected after the analysis in Sec. IV A.

### A. Relaxed Clusters

In cluster physics is common to describe atoms as hard spheres, and to use them as a linear length unit. Following this idea, in the micro-crystal size regime (where a high rate of the total  $N$  atoms belong to the bulk) the particles are  $N^{1/3}$  atoms long, with area facets proportional to  $N^{2/3}$  atoms. Only some atoms belong to the surface ( $\sim N^{2/3}$ ), located predominately on the facets and only a negligible number on the edges and the vertices. On the contrary, when the cluster size is decreased, almost all the atoms tend to be at the surface. In this case, however, the amounts of atoms in the edges, the vertices, and the facets tend to compete among them, and the extreme case is for the very smaller clusters that contains only vertex atoms. Therefore, it would be helpful to obtain a function that give insights in which range of  $N$ , the macro/micro ( $N_{\text{surf}} \ll N$ ) or the nano ( $N_{\text{surf}} \approx N$ ) character of any studied cluster is manifested.

For this purpose, it is proposed a function for the number of surface atoms  $N_{\text{surf}}$ , in terms

TABLE II: The parameters for the fitting function, Eq. (7), together with its asymptotic standard errors for the SC and SI gold clusters relaxed with the steepest-descents and the CR potential model.

	$\alpha$	$\beta$	$\gamma$
SC	$6.4490 \pm 0.0005$	$-13.97 \pm 0.01$	$9.33 \pm 0.08$
SI	$8.4663 \pm 0.0006$	$-39.74 \pm 0.02$	$73.15 \pm 0.11$

of  $N^{1/3}$ ,  $N^{2/3}$ , and a constant, as follows

$$N_{\text{surf}}(N) = \alpha N^{2/3} + \beta N^{1/3} + \gamma, \quad (7)$$

where the coefficients  $\alpha$ ,  $\beta$ , and  $\gamma$  must be free parameter, since the function must describe the full number of surface atoms for small, intermediate, and large size clusters. Thus, when fitting the function to data a high correlation between them is expected and some of them could get negative values.

The behavior of the computed ratio,  $N_{\text{surf}}/N^{2/3}$ , as a function of the cluster size, is almost the same for both the relaxed and unrelaxed SI and SC clusters, as is shown in Fig. 5. The number of surface atoms of each relaxed cluster,  $N_{\text{surf}}$ , has been calculated through the Lee–Richard algorithm<sup>35</sup> using the Van der Waals radius of gold as a probe radius  $r_{\text{probe}} = 1.66 \text{ \AA}$ . Hereafter we denote this function as  $\mathcal{N}(N) = N_{\text{surf}}/N^{2/3}$  in order to facilitate discussions. In the Figure, the solid and dotted lines are obtained by linear fitting of SC and SI  $N_{\text{surf}}$  data to functions of the form given by Eq. (7), respectively. Here the function  $\mathcal{N}_{\text{SC}}(N)$  is for  $N \geq 21$ , while  $\mathcal{N}_{\text{SI}}(N)$  is for  $N \geq 135$ . The coefficients of the fitting functions for the SC and SI clusters are given in Table II. Note that some parameters are necessarily negative.

As can be seen from Fig. 5, calculated values for SC clusters tend faster to its asymptotic value,  $\alpha_{\text{SC}} = +6.449$ , than those values for SI clusters, that tend to  $\alpha_{\text{SI}} = +8.466$ . The asymptotic value  $\alpha_{\text{SC}}$  is greater than the asymptotic value for a simple cubic cluster,  $\alpha_{\text{cubic}} = 6.0$ , since the *SC* clusters are based on a truncated fcc with tetrahedral units attached to the (111) faces. The value  $\alpha_{\text{SI}} = +8.466$  is explained by a similar reasoning. For cluster sizes of  $O(10^6)$ , values of the fitting functions  $\mathcal{N}_{\text{SC}}$  and  $\mathcal{N}_{\text{SI}}$  are around the 2.2% and 4.6% of their asymptotic values, respectively. Thus, one could expect stronger surface effects for SI clusters than for the SC clusters, or one could expect that the SC clusters already behave

as macro clusters ( $N_{\text{surf}} \propto N^{2/3}$ ) for relatively small sizes,  $N \sim 10^6$ , so that many properties of SC could be dominated by volume atoms. For SI clusters in the same range one could expect properties dominated by surface atoms. As a note of caution, the stellated clusters have very specific sizes, see Eqs. (6), because they are constructed using complete tetrahedral units mounted on the eight triangular faces of the cuboctahedra or over the twenty faces of the icosahedral clusters. Hence, detailed interpolation or extrapolations results from Eq. (7) must be taken with care.

In the small size range, the stellated clusters with sizes  $N_{\text{SC}}(4) = 469$  and  $N_{\text{SI}}(4) = 709$  contain tetrahedral units of 20 atoms, and interesting is to note that tetrahedral gold cluster with 20 atoms have been proven to be the more stable gold isomer<sup>36</sup>. To this respect, we also note that after the slightly relaxation processes, where each of the potential models displayed in Table I were used, we have observed that the shape of each cluster in Fig. 4 is maintained; the relaxed clusters are contracted in the average, as it is expected for these kind of potential models<sup>16</sup>, being more evident this result in the smaller ones due to the high value of the surface/volume ratio, but the peaks of all the clusters are maintained, which can be attributed to the same mechanism that maintains vertex atoms of the global minima tetrahedral cluster of Fernandez *et al.*<sup>36</sup>.

In order to explore the energetic trends of the relaxed SC and SI clusters under the potential models given in Table I, we have first fitted the potential energy data of each series to a function of the form (see Ref. 15 and references therein)

$$E(N) = AN + BN^{2/3} + CN^{1/3} + D, \quad (8)$$

where the coefficient  $A$  is proportional to the energy per atom of the bulk-like atoms, that follows from the asymptotic behavior of  $E(N)/N$  for large clusters. The number of bulk atoms is taken proportional to the cluster size  $N$ . Thus, at least for large clusters, the first term in the Equation could be interpreted as the contribution to total energy due to bulk atoms, and the last three term together as the contribution to total energy due to the atoms at the surface. The explicit dependence on  $N^n$  (1/3, 2/3, and 0) comes from the splitting of the full number of surface atoms into facets atoms (proportional to  $N^{2/3}$ ), edges atoms (proportional to  $N^{1/3}$ ), and vertexes atoms, a constant.

Therefore, by construction, the first term in Eq. (8) is interpreted as the total volume contribution to the energy, and the second, third, and fourth terms together are interpreted

TABLE III: The coefficients for the fitting function, Eq. (8), for the steepest-descents relaxed SC (first row) and SI (second row) clusters with the potential models given in Table I. Units are eV/atom.

Model	$A$	$\sigma^a$	$B$	$C$	$D$
CR	$-3.7795 \pm 0.0003$	0.0000	$1.570 \pm 0.007$	$-0.71 \pm 0.06$	$1.68 \pm 0.11$
	$-3.7687 \pm 0.0002$	0.0108	$1.678 \pm 0.003$	—	$-3.53 \pm 0.05$
RGL	$-3.8256 \pm 0.0002$	0.0000	$1.454 \pm 0.007$	$-0.73 \pm 0.05$	$1.76 \pm 0.10$
	$-3.8160 \pm 0.0002$	0.0096	$1.554 \pm 0.003$	—	$-3.21 \pm 0.04$
BFFMM	$-3.8284 \pm 0.0002$	0.0000	$1.436 \pm 0.005$	$-0.77 \pm 0.04$	$1.84 \pm 0.08$
	$-3.8186 \pm 0.0002$	0.0099	$1.533 \pm 0.004$	—	$-3.16 \pm 0.05$
CP	$-3.7600 \pm 0.0001$	0.0000	$2.967 \pm 0.004$	$-0.54 \pm 0.03$	$0.34 \pm 0.06$
	$-3.7336 \pm 0.0013$	0.0264	$3.125 \pm 0.021$	—	$-7.87 \pm 0.29$

<sup>a</sup> $\sigma = A - E_{\text{ref}}$ , where  $E_{\text{ref}} = A_{\text{SC}}$ .

as the total surface energy contribution (see Ref. 15 for details). As in the case of  $N_{\text{surf}}(N)$ , see Eq. (7), the coefficients in Eq. (8) must be free parameters, and high correlation among them are expected (mainly among coefficients B, C, and D) when fitting data of small, intermediate or large size clusters to this equation.

The parameters for the fit to each type of stellated clusters and potential models are given in Table III. To avoid large asymptotic standard errors in the linear fitting data of SI clusters, the coefficient C is excluded from its fitting process. Note that, for the potential models RGL and BFFMM, the asymptotic values for the binding energy,  $A_{\text{SC}}$ , are lower than the experimental cohesive energy of bulk used in the parameterization of each of the potential model (see Table I), however they are very close to the experimental cohesive energy,  $E_{\text{coh}} = -3.81$  eV/atom reported in Ref. 37. For the CP model  $A_{\text{SC}}$  is exactly the calculated value of the cohesive energy of bulk Au reported by Chamati and Papanicolaou<sup>26</sup>, and for the CR model the value of  $A_{\text{SC}}$  is very close to the experimental cohesive energy of bulk used in its parameterization<sup>19</sup>.

In order to explore which type of relaxed structure is more favorable, we have used as

diagnostic tool the excess energy per  $N^{2/3}$ , defined by<sup>15</sup>,

$$\Delta(N) = \frac{E - NE_{\text{ref}}}{N^{2/3}}; \quad (9)$$

where  $E$  stands for the total potential energy of one cluster of size  $N$ , and it is common to take for the reference energy  $E_{\text{ref}}$  the experimental cohesive energy of the bulk used in the parameterization of the potential model, see Table I. Here, for each potential model,  $\Delta(N)$  is calculated using  $E_{\text{ref}} = A_{SC}$ , where  $A_{SC}$  is given in Table III. The results of the calculations of  $\Delta(N)$  using each of the potential models in Table I and the steepest-descents method are given in Fig. 6. It can be observed from this figure that at this stage of the simulations, almost all SC clusters, except  $N_{SC}(1) = 21$ , are more favorable than the SI clusters. This behavior occurs for all potential models, except the CP model which also excludes  $N_{SC}(2)$ . Similar results have been found by Baletto et al.<sup>25</sup>, using the RGL and embedded-atom models, but for non-stellated icosahedral and cuboctahedral clusters. However, as can be seen from the calculated data in the figure, the effects of mounting tetrahedral motifs on the triangular faces of cuboctahedral or icosahedral clusters changes significantly the behavior of  $\Delta(N)$ . For instance,  $\Delta$  data of icosahedral clusters in Ref. 25 is concave up, while the  $\Delta$  data of SI clusters in Fig. 6 is concave down. For Lennard-Jones icosahedral and fcc cluster data<sup>38,39</sup>, it has been found that  $\Delta$  is concave down for both types of clusters. We have explored the concavity effect by expressing  $\Delta(N)$  in the form

$$\Delta(N) = \sigma N^{1/3} + B + C/N^{1/3} + D/N^{2/3}, \quad (10)$$

which follows using Eq. (8) into Eq. (9). The parameter  $\sigma = A - E_{\text{ref}}$  is interpreted as the strain or elastic energy per atom of the cluster<sup>15,39,40</sup>. It is well known that for clusters with fcc symmetry,  $\sigma_{\text{fcc}}$  is negligible since the bulk energy per atom  $A_{\text{fcc}}$ , is the optimum. On the contrary, it is also well known that the non-crystalographic symmetry of the clusters frustrates the elimination of strains by the minimization process, and consequently they can accumulate that energy as elastic-energy<sup>15,39,40</sup>, which increases with cluster size. In principle,  $A$  must be higher or equal to the cohesive energy of the bulk crystal,  $E_{\text{coh}}$ , which can be appreciated as the optimum energy per atom of volume atoms; however in practice, when fitting MDS results to Eq. (8),  $A$  could be slightly lower than  $E_{\text{coh}}$ . This could be attributed to the linear fitting of MDS data, and or to the cut-off radius used in the interactions: in all potential models we have included more than one coordination shell in the interactions. In

any case, since one is interested in the relative stability of the two types of clusters, to avoid negative values for  $\sigma$  in Eq. (10) we have used for the reference energy  $E_{\text{ref}}$  the lower value for  $A$  in each potential model, instead of the experimental cohesive energy of bulk used in the parameterization of the potential model, see Table. I.

In Fig. 6, the solid and dotted lines in each plot are the curves  $\Delta_{\text{SC}}(N)$  and  $\Delta_{\text{SI}}(N)$  obtained from Eq. (10) with the coefficients given in Table III, for the potential models CR (a), CP (b), RGL (c), and BFFMM (d). Note that, in general, the asymptotic value for the binding energy  $A_{\text{SC}}$ , is lower than the experimental cohesive energy of bulk used in the parameterization of the potential model, see Table I. As pointed out in the preceding paragraph, to avoid negative values of  $\sigma_{\text{SC}}$ , we have used  $E_{\text{ref}} = A_{\text{SC}}$  in the Eq. (10) for the SC and SI clusters. This procedure has not effect in the present analysis, since only we have changed the reference point of energy. For all the potential models the respective functions,  $\Delta_{\text{SC}}(N)$  and  $\Delta_{\text{SI}}(N)$ , predict only one crossover size. Only the crossover sizes for the RGL, BFFMM, and CR models agree with the rule: the larger is  $pq$ , the smaller are the crossover sizes<sup>15,25</sup>. The CP model has the higher value of  $pq$ , and also the higher value of the crossover size. The exact values of the crossover sizes have no real significance, since the calculations have been limited to clusters sizes given in Eqs. 6. We only could infer from these results that both types of clusters could coexists around these sizes. For any potential model, no others crossover sizes occur for the larger clusters of both types, since their asymptotes, right lines in  $\Delta(N^{1/3})$ , are not intersected. Thus, each one of the potential models predict only one crossover size, which occurs for relatively small cluster sizes. Therefore, at this stage of the MD simulations we could partially conclude that (a) all the slightly relaxed structures maintain the star-like shape of the initial structures; (b) all SC clusters, except the smaller cluster, are more favorable than the SI clusters; (c) the most strained SI structures are given by the CP model, and the less strained are given by the RGL model (elastic energy values given by the CR and BFFMM models are very close to the value given by the RGL model); and (d) only the asymptotic value for the binding energy  $A_{\text{SC}}$ , given by the CR model, is very close to the value of the experimental cohesive energy used in its parameterization.

## B. Equilibrated Clusters at $T = 298$ K

MD simulations at room temperature of the relaxed clusters described above have been conducted as follows: for each cluster a sample of mechanical states of length 0.25 ns has been produced in a weak-ensemble approximating the microcanonical-ensemble ( $\alpha \simeq 1$ ), and after 2 ns of equilibration length. This procedure has been applied to each cluster in the range  $21 \leq N \leq 3095$ , including  $N = 5631$  and  $N = 6169$ , and except those with sizes  $N_{\text{SC}} = 9437$  and  $N_{\text{SI}} = 10803$ , where an equilibration length of 1 ns was used. In the equilibration period, the Berendsen's thermostat with time-coupling parameter  $\tau_T = 0.4$  ps and target temperature  $T_0 = 298$  K was used<sup>32,33</sup>. In all the simulations a time-step of 1 fs is used, and periodic boundary conditions has been applied, but with a much larger box length than the cluster radius to ensure non-interacting images. A cutoff radius equal to half box length was used for clusters sizes  $N \leq 87$ , otherwise a cutoff radius of 2 nm was set. Statistical properties of the produced sampled distribution were obtained using the coarse-graining stratified systematic sampling dividing the sample in equal bins of length 0.05 ps, to avoid serial correlations. The averages of the properties considered in this work are reported at the 95% of confident level. All simulation results have been obtained using only the CR potential model, since the asymptotic behavior of  $E(N)/N$  for the relaxed SC clusters reproduces very well the experimental cohesive energy used in the parameterization of the model.

As it can be observed from the average equilibrium configurations of the two series of clusters shown in Fig. 7, one of the more evident temperature effects on clusters for sizes  $347 < N < 9437$  is the smoothing of all the peaks of the tetrahedral pyramidal motifs of the relaxed clusters. This is easy to understand due to the natural tendency of lower coordinated surface atoms to increase its coordination number to the optimum value, which in this case is driven by thermal energy. For the first three clusters of each series we have found that all the peaks are completely destroyed in agreement with recent results, which shown that small gold clusters are low-symmetry or amorphous-like clusters<sup>40</sup>. By the other hand, for the two largest clusters of each series, Figs. 11, some peaks remain due mainly to the length of 1 ns used in its equilibration period. Their contribution to the energy could be neglected since, as we will show below, volume contribution dominates over surface contributions at these sizes. Eventually, it is expected these peaks are finally smoothed if equilibration length

TABLE IV: Same as Table II, but for the equilibrated gold clusters with the CR potential model.

	$\alpha$	$\beta$	$\gamma$
SC	$6.41 \pm 0.02$	$-13.07 \pm 0.33$	—
SI	$8.44 \pm 0.03$	$-37.32 \pm 0.50$	—

is extended to 2 ns. Thus, the surfaces of our equilibrated clusters at room temperature for sizes in the range  $347 < N \leq 10803$  resembles the TEM images of the gold particles (a), (b) and (d) in Fig. 2.

By following the equilibration time history of clusters with sizes greater than 347 atoms, we have observed in detail how the peaks of the pyramids are smoothed. For any cluster at the initial steps of the equilibration process, each pyramid tip atom is diffused along one edge and it attaches around the middle edge for long time, generating metastable states. After a short period, these atoms remove (almost always) another atoms from those mid edge positions, that are rolled towards the base of the pyramid, and the total energy is stabilized for longer periods, which might be considered as an stable state. For the SC clusters, we have found that those atoms form oscillating pairs of atoms, which are deposited on the surface around vertices connecting square faces. Nowdays, there are high interest on the collective electronic excitations or surface plasmons of star-like gold nanoparticles, and these theoretical findings could give some insights on the features of the collective electronic excitations resulting from the interaction of star-like nanoparticles with the electric field of light<sup>41–44</sup>.

From the above results on equilibrated surface atoms, minimal changes in the behavior of the number of surface atoms as a function of cluster size are expected, and this is indeed the case if the curves  $\mathcal{N}(N)$  for the SC and SI clusters on Fig. 5 are compared with those of the equilibrated clusters shown in Fig. 8. The behavior of the corresponding curves, for  $N > 347$ , is very similar. As in the case of the relaxed clusters described in the preceding section, curves in Fig. 8 have been obtained by linear fitting  $N_{\text{surf}}$  to Eq. (7), where  $N_{\text{surf}}$  is the number of surface atoms of the average equilibrium configurations shown in Fig. 7. The coefficients of the fitting functions for the equilibrated SC and SI clusters are given in Table IV, where the coefficient  $\gamma$  has been excluded from the fitting process in order to avoid large asymptotic standard errors in the coefficients. Since the main interest here is on the large stellated

TABLE V: Same as Table III, but for the equilibrated gold clusters with the CR potential model.

Cluster type	$A$	$\sigma^a$	$B$	$C$	$D$
SC	$-3.6982 \pm 0.0006$	0.0151	$1.496 \pm 0.012$	–	$-1.64 \pm 0.54$
SI	$-3.7132 \pm 0.0040$	0.0000	$2.545 \pm 0.107$	$-8.22 \pm 0.63$	–

<sup>a</sup> $\sigma = A - E_{\text{ref}}$ , where  $E_{\text{ref}} = A_{\text{SI}}$ .

structures which maintain their peaks, the first three equilibrium configurations of each series have been excluded from the fitting, and also from the discussions, since they are amorphous or low-symmetry structures described in detail by Soler *et al.*<sup>40</sup>. From Fig. 8, the number of surface atoms of the SI clusters is lower than for relaxed clusters; on the contrary, relaxed and equilibrated SC clusters have almost the same number of surface atoms. For large clusters, the asymptotic behavior of dotted curves, or solid curves, is very similar. Thus, from the energetic point of view, details of the surface atoms of very large particles could not be important since volume atoms dominate energy contributions, but the smoothed peaks of the clusters can play a significant role in the description of the surface plasmons of these nanoparticles.

By following the same procedure as for the relaxed clusters, we have also explored which type of equilibrated gold cluster is more favorable. In this case  $E$  in Eq. (9) is the total energy of a cluster of size  $N$ ,  $N_{\text{surf}}$  is given by Eq. (7) and Table IV, and for  $E_{\text{ref}}$  we have used  $A_{\text{SI}} = -3.7132$  eV/atm given in Table V. The calculated values for  $\Delta_{\text{SC}}(N)$  and  $\Delta_{\text{SI}}(N)$  are given in Fig. (9) together with its fitted curves, where the coefficients are given in Table V. In this case only  $E(N)$  data for  $N \geq 347$  has been fitted to Eq. (8), and to avoid large asymptotic errors in the coefficients,  $C$  and  $D$  have been omitted in the fitting process of data  $E_{\text{SC}}(N)$  and  $E_{\text{SI}}(N)$ , respectively. From interpolation and extrapolation results we have found that the SC clusters are more favorable in the range  $671 \lesssim N \lesssim 224\,586$ , while SI clusters are more favorable out of this range, excluding the first five smaller clusters. Thus, we predict that stellated gold clusters coexist around two crossover sizes; one at  $N \simeq 671$  and another one at  $N \simeq 224\,586$ , a result that is well agreement with experimental facts (see Fig. 2).

## V. CONCLUSIONS

We have synthesized and characterized by TEM stellated gold nanoparticles, as well as performed a systematic study for their structure and energetic stability through geometrical models and by means of molecular dynamics simulations at room temperature. From the analysis of the MDS results, we can conclude that: (a) the morphology and the surface structure of these stellated clusters for sizes  $N > 347$  are in good agreement with the synthesized NPs, as well as with the results reported recently by Burt *et al.*<sup>2</sup>. The structure of peaks is maintained and the coexistence of the two type of particles has been demonstrated. Smaller clusters are low-symmetry or amorphous structures already studied in Ref. 40; (b) the stellated gold clusters prefer SC tructures for cluster sizes in the range  $347 < N < 226281$  ( $\approx 30$  nm), where surface effects are stronger for SI clusters than for SC clusters; in fact the behavior of  $\mathcal{N}_{\text{SC}}(N^{1/3})$  is almost lineal. We predict that around a cluster size of 30 nm, both types of clusters could coexist, and for larger clusters the SI structure is more favorable than the SC structure. Finally, it is important to emphasize that we are comparing clusters of different size which have cores of the same size, cuboctahedral or icosahedral clusters with same magic size, thus this difference in the number of atoms arises from the tetrahedral motifs attached to their triangular faces.

The present study on stellated gold nanoparticles is driven mainly by fundamental and applied *leit motivs*. From the fundamental point of view, we advanced the hypothesis that stellation on clusters (Kepler-Poisont solids) is a process that follows after the nucleation of well defined structures, such as octahedra and icosahedra (platonic shapes) and cuboctahedra and truncated octahedra (archimedean solids), where each one of these shape classifications could be (althought with not well defined boundaries) located in size regions of the cluster growth. From the applied point of view, stellated gold nanoparticles have nowadays and projected in the near future, potential nanotechnological applications in disciplines such as the biomedical applications (cell tissue imaging, sensing and cancer therapy, drug delivery, etc.)<sup>11-14</sup>, and nanophotonics applications<sup>41-44</sup>.

## Acknowledgments

This work has been supported by FAI-UASLP (grant C07-FAI-04-21.23), PIFI-2008 (grants 24MSU0011E-06 and 24MSU0011E-05), and CONACYT grant 106437; the Welch Foundation with grant number AX-1615 and the National Science Foundation (NSF) project number DMR-0830074. We also acknowledge Prof. J.A. Alonso (U. Valladolid, España) for critical reading and comments on the manuscript. Finally, authors acknowledge high performance computational resources granted by the Centro Nacional de Supercómputo (CNS-IPICYT).

---

\* Electronic address: [cabrera@fc.uaslp.mx](mailto:cabrera@fc.uaslp.mx)

† Electronic address: [jlrdz@ipicyt.edu.mx](mailto:jlrdz@ipicyt.edu.mx)

<sup>1</sup> J.L. Rodríguez-López, J.M. Montejeno-Carrizales, and M. José-Yacamán, *Modern Phys. Lett. B* **20**, 725 (2006).

<sup>2</sup> J. L. Burt, J. L. Elechiguerra, J. Reyes-Gasga, J. M. Montejano-Carrizales, and M. José-Yacamán, *J. Crys. Growth* **285**, 681 (2005).

<sup>3</sup> D. Senapati, A.K. Singh, and P. Chandra-Ray, *Chem. Phys. Lett.* **487**, 88 (2010).

<sup>4</sup> Hsin-Lun Wu, Chiu-Hua Chen, and Michael H. Huang, *Chem. Mater.* **21**, 110 (2010).

<sup>5</sup> H. Hofmeister, *Z. Kristallogr.* **224**, 528 (2009).

<sup>6</sup> Y. Xia, Y. Xiong, B. Lim, and S.E. Skrabalak, *Angew. Chem. Int. Ed.* **48**, 60 (2009).

<sup>7</sup> T.K. Sau, A.L. Rogach, F. Jäckel, T.A. Klar, and J. Feldmann, *Adv. Mater.* **21**, 1 (2009).

<sup>8</sup> C.J. Murphy, *et al.*, *J. Phys. Chem. B* **109**, 13857 (2005).

<sup>9</sup> A. Sánchez-Iglesias *et al.*, *Adv. Mater.* **18**, 2529 (2006).

<sup>10</sup> C. Noguez, *J. Phys. Chem. C* **111**, 3806 (2007).

<sup>11</sup> Prashant K. Jain, Kyeong Seok Lee, Ivan J. *Phys. Chem. B* **110**, 7238 (2006).

<sup>12</sup> X. Huang, Ivan H. El-Sayed, Wei Qian, and Mostafa El-Sayed, *J. Am. Chem. Soc.* **128**, 2115 (2006); Cancer

<sup>13</sup> Q. Wei, H.-M. Song, A.P. Leonov, J.A. Hale, D. Oh, Q.K. Ong, K. Ritchie, and A. Wei, *J. Am. Chem. Soc.* **131**, 9728 (2009).

<sup>14</sup> Hugh H. Richardson *et al.*, *NanoLett.* **6**, 783 (2006); *idem* **9**, 1139 (2009).

<sup>15</sup> F. Baletto and R. Ferrando, *Rev. Mod. Phys.* **77**, 371 (2005).

<sup>16</sup> R. P. Gupta, *Phys. Rev. B* **23**, 6265 (1981).

<sup>17</sup> D. Tománek, A. A. Aligia, and C. A. Balseiro, *Phys. Rev. B* **32**, 5051 (1985).

<sup>18</sup> V. Rosato, M. Guillope, and B. Legrand, *Philos. Mag. A* **59**, 321 (1989).

<sup>19</sup> F. Cleri and V. Rosato, *Phys. Rev. B* **48**, 22 (1993).

<sup>20</sup> M. W. Finnis and J. E. Sinclair, *Philos. Mag. A* **50**, 45 (1984).

<sup>21</sup> M. S. Daw and M. I. Baskes, *Phys. Rev. B* **29**, 6443 (1984).

<sup>22</sup> J. M. Montejano-Carrizales, J. L. Rodríguez-López, C. Gutierrez-Wing, M. Miki-Yoshida, and M. José-Yacamán, *Crystallography and Shape of Nanoparticles and Clusters* (American Sci-

entific Publishers, Stevenson Ranch, Calif, 2004), vol. 2 of *Encyclopedia of Nanoscience and Nanotechnology*, pp. 237–282, 1st ed.

<sup>23</sup> F. H. Stillinger and T. A. Weber, Phys. Rev. A **25**, 978 (1982).

<sup>24</sup> R. L. Johnston, Dalton Trans. **22**, 4193 (2003).

<sup>25</sup> F. Baletto, R. Ferrando, A. Fortunelli, F. Montalenti, and C. Mottet, J. Chem. Phys. **116**, 3856 (2002).

<sup>26</sup> H. Chamati and N. I. Papanicolaou, J. Phys.: Condens. Matter **16**, 8399 (2004).

<sup>27</sup> M. J. López and J. Jellinek, J. Chem. Phys. **110**, 8899 (1999).

<sup>28</sup> C. Kittel, *Introduction to Solid State Physics* (John Wiley & Sons, Inc., 1976), 5th ed.

<sup>29</sup> W. R. P. Scott, P. H. Hunenberger, I. G. Tironi, A. E. Mark, S. R. Billeter, J. Fennen, A. E. Torda, T. Huber, P. Kruger, and W. F. van Gunsteren, J. Chem. Phys. A **103**, 3596 (1999).

<sup>30</sup> M. P. Allen and D. J. Tildesley, *Computer Simulation of Liquids* (Oxford University Press, Inc., New York, 1997).

<sup>31</sup> N. T. Wilson, Ph.D. thesis, University of Birmingham (2000).

<sup>32</sup> H. J. C. Berendsen, J. P. M. Postma, W. F. van Gunsteren, A. DiNola, and J. R. Haak, J. Chem. Phys. **81**, 3684 (1984).

<sup>33</sup> T. Morishita, J. Chem. Phys. **113**, 2976 (2000).

<sup>34</sup> I. L. Garzón, K. Michaelian, M. R. Beltrán, A. Posada-Amarillas, P. Ordejón, E. Artacho, D. Sánchez-Portal, and J.M. Soler, *Phys. Rev. Lett.* **81**, 1600 (1998).

<sup>35</sup> B. Lee and F. M. Richards, J. Mol. Biol. **55**, 379 (1971).

<sup>36</sup> E. M. Fernández, J. M. Soler, I. L. Garzón, and L. C. Balbás, Phys. Rev. B **70**, 165403 (2004).

<sup>37</sup> C. Kittel, *Introduction to Solid State Physics* (John Wiley & Sons, Inc., 1995), 7th ed.

<sup>38</sup> J. Xie, J. A. Northby, D. L. Freeman, and J. D. Doll, J. Chem. Phys **91**, 612 (1989).

<sup>39</sup> J. A. Northby, J. Xie, D. L. Freeman, and J. D. Doll, Z. Phys D **12**, 69 (1989).

<sup>40</sup> J. M. Soler, M. R. Beltrán, K. Michaelian, I. L. Garzón, P. Ordejón, D. Sánchez-Portal, and E. Artacho, Phys. Rev. B **61**, 5771 (2000).

<sup>41</sup> V. Giannini, R. Rodríguez-Oliveros, and J.A. Sánchez-Gil, *Plasmonics* **5**, 99 (2010)

<sup>42</sup> C. Hrelescu, T.K. Sau, A.L. Rogach, F. Jäckel, and J. Feldmann, *Appl. Phys. Lett* **94**, 153113 (2009).

<sup>43</sup> P. Senthil-Kumar, I. Pastoriza-Santos, B. Rodríguez-González, F.G. García de Abajo, and L.M. Liz-Marzán, *Nanotechnology* **19**, 015606 (2008).

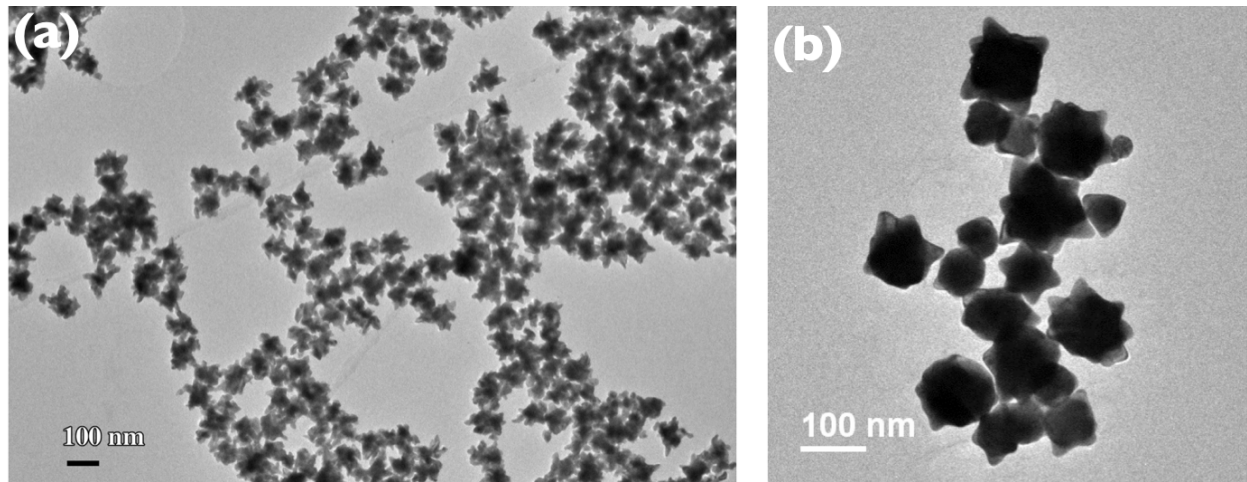


FIG. 1: (a) Low resolution transmission electron microscopy image of gold nanoparticles with a high production rate of stellated particles. In (b) a magnified region where more detail of these stellated clusters is observed.

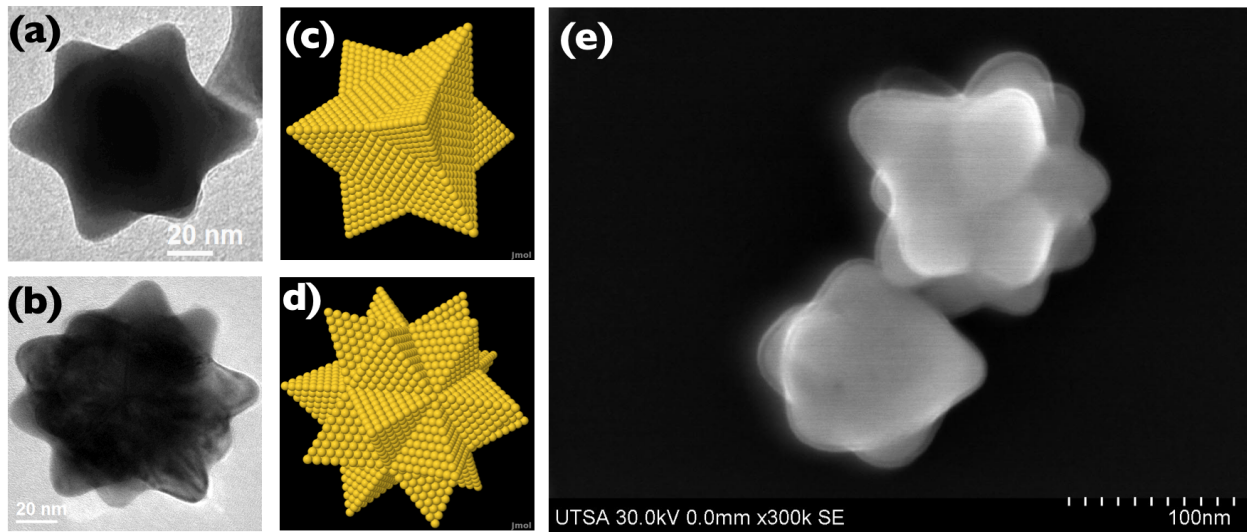


FIG. 2: Transmission electron microscopy images of gold particles with assumed (a) cuboctahedral and (b) icosahedral seeds. Models that resemble these images are shown in (c) and (d). SEM image in (d) evidence both kind of stellated clusters coexisting.

<sup>44</sup> C.L. Nehl, H. Liao, and J.H. Hafner, *NanoLett.* **6**, 683 (2006).

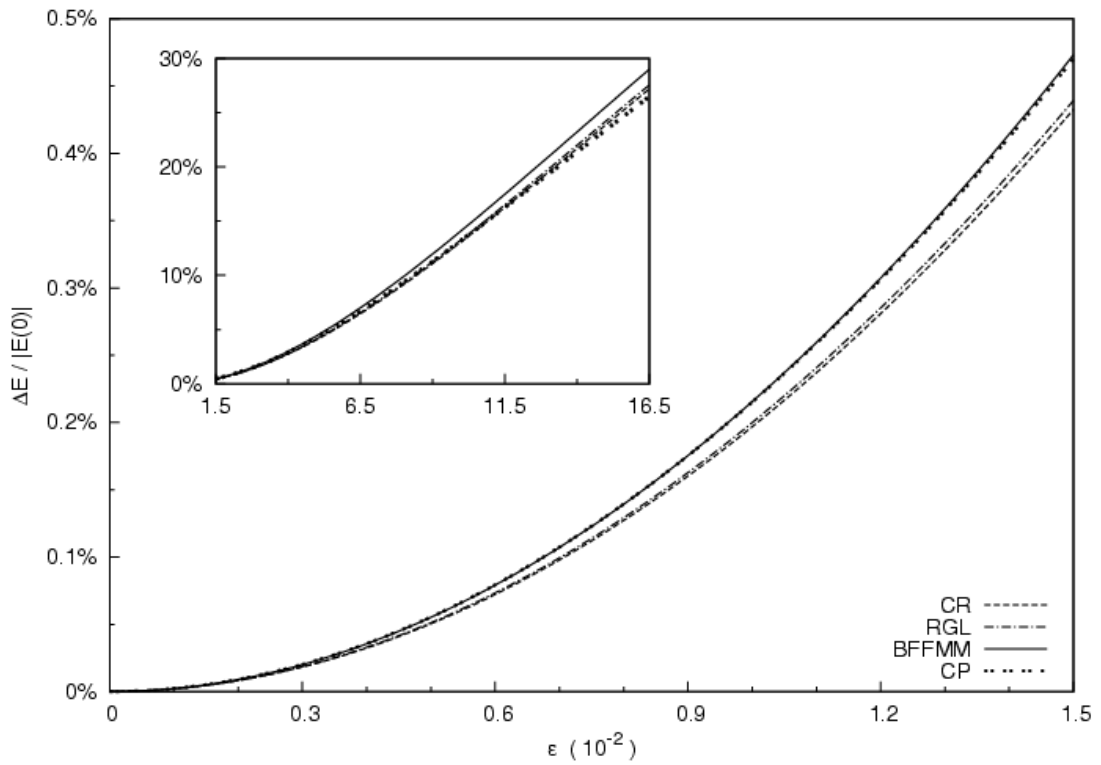


FIG. 3: Behavior of the fractional change in the cohesive energy accompanying a fractional change in the first nearest-neighbors distance  $\epsilon = (r_{ij} - r_0)/r_0$  as given by Eq. (4) for the potential models given in Table I.

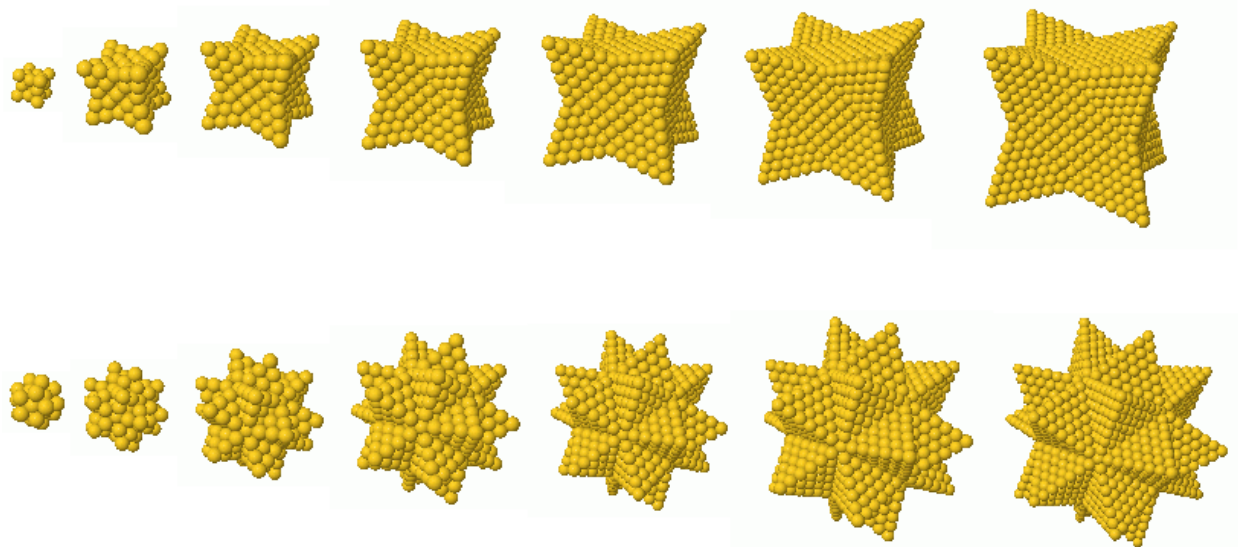


FIG. 4: Some star-like gold clusters, similar to those shown in Fig. 2, where each one was obtained by using regular tetrahedral motifs attached to the eight (111) faces of a cuboctahedron (top row) or the twenty (111) faces of the icosahedron (bottom row), both with magic size. These piñata-like clusters correspond, from left to right, to  $k = 1, 2, 3, \dots, 7$ , see Eqs. (6).

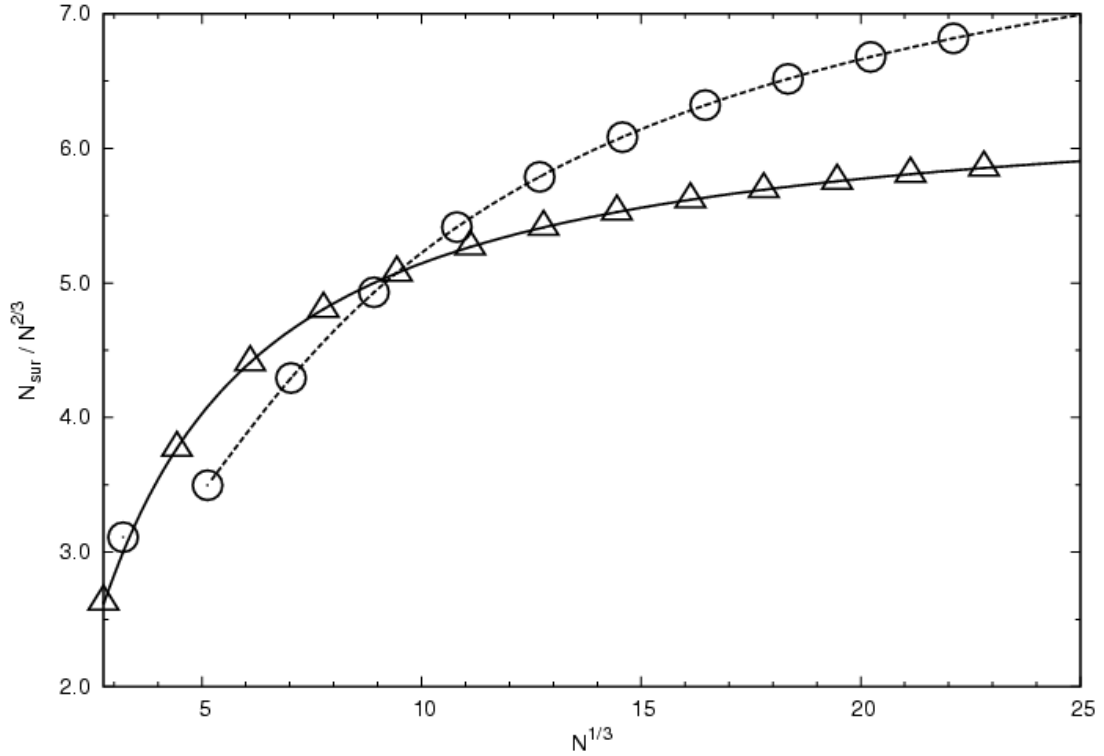


FIG. 5: Behavior of the ratio  $N_{\text{surf}}/N^{2/3}$  as function of  $N^{1/3}$ , where  $N$  is the cluster size, for both the relaxed SC ( $\triangle$ ), and SI ( $\circ$ ) clusters, see Fig 4. The actual number of surface atoms of each stellated cluster,  $N_{\text{surf}}$ , is calculated through the Lee-Richard algorithm<sup>35</sup> using a probe radius  $r_{\text{probe}} = 1.66$  Å. The dashed and solid lines are obtained by fitting the corresponding  $N_{\text{surf}}$  data to Eq. (7). Note that the smaller cluster of the SI series is excluded from the fitting.

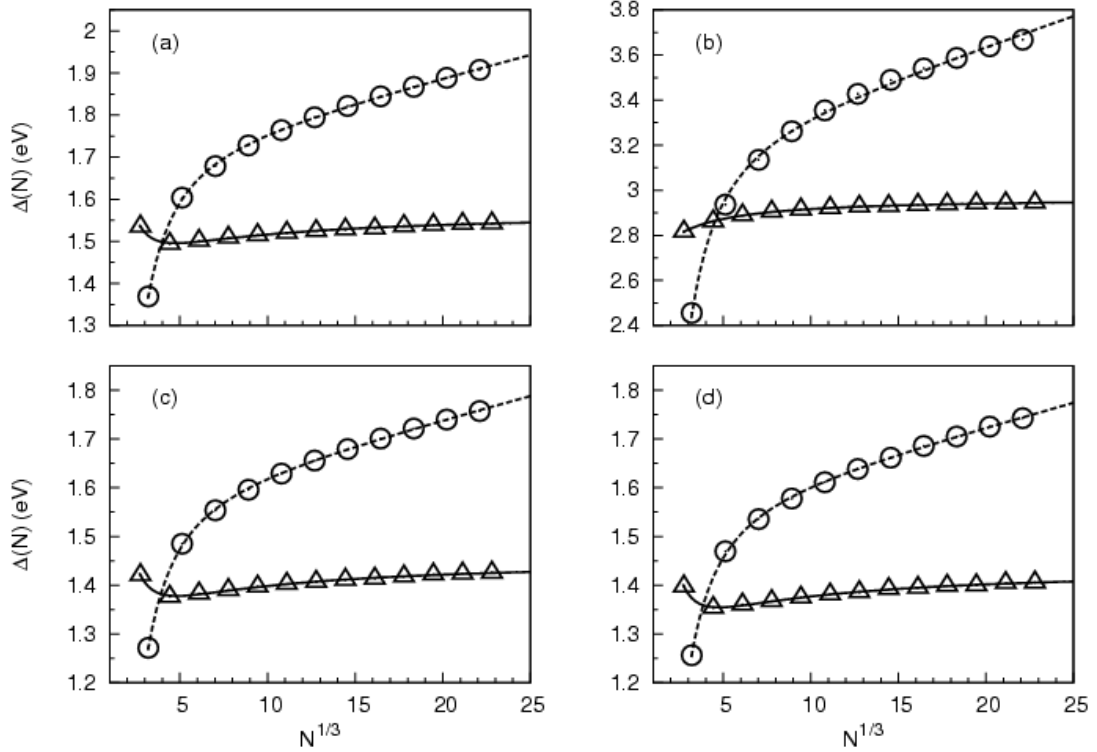


FIG. 6: Trends of the calculated excess energy per  $N^{2/3}$ ,  $\Delta(N)$ , as function of  $N^{1/3}$ , for both SC ( $\triangle$ ), and SI ( $\circ$ ) relaxed clusters for the potential models CR (a), CP (b), RGL (c), and BFFMM (d). The solid and dotted lines are the curves  $\Delta_{SC}(N)$ , and  $\Delta_{SI}(N)$  from Eq. (10), where the coefficients are given in Table III, respectively. For each potential model  $E_{ref} = A_{SC}$  has been used.

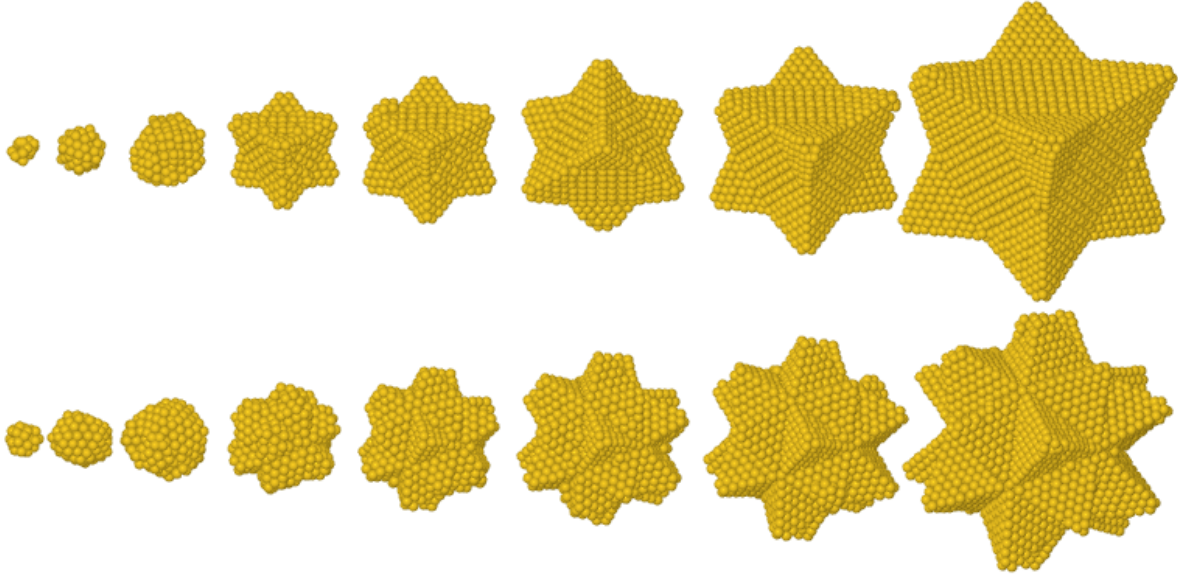


FIG. 7: Same as Fig. 4, but for the average equilibrium configurations of the stellated gold clusters obtained by MDS at room temperature. First row are those gold clusters based on initial structures with cuboctahedral core, and second row those with icosahedral core. The first three clusters of each series ( $k = 1, 2, 3$ ) are structures of low-symmetry or amorphous-like clusters<sup>34,40</sup>. The last cluster in each series corresponds to  $N_{\text{SI}}(9) = 6169$  (bottom), and  $N_{\text{SC}}(10) = 5631$  (top).

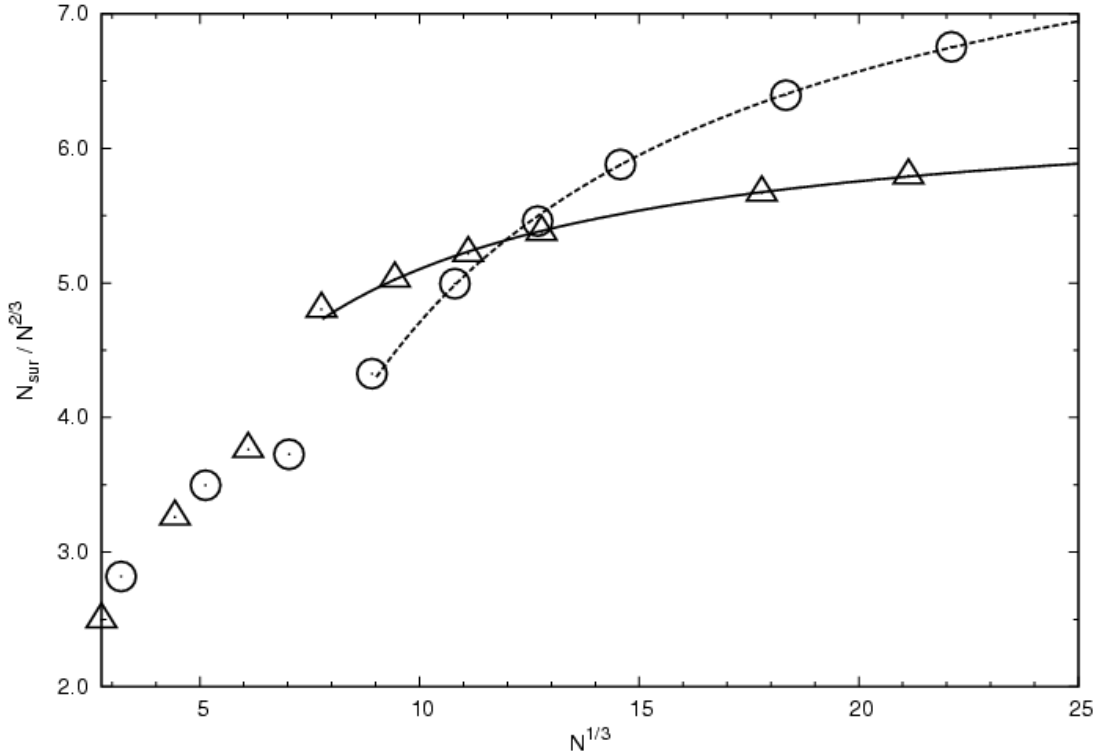


FIG. 8: Same as Fig. 5, but for the average equilibrium configurations shown in Fig. 7 and Fig. 11. In this case only the  $N_{\text{surf}}$  data, for  $N \geq 469$  has been fitted to Eq. (7) excluding the coefficient  $\gamma$ ; the first three clusters of each series are excluded from the fitting, since they are amorphous or low-symmetry structures<sup>34,40</sup>.  $N_{\text{surf}}$  has also been computed through the Lee-Richard algorithm<sup>35</sup> using a probe radius  $r_{\text{probe}} = 1.66 \text{ \AA}$ .

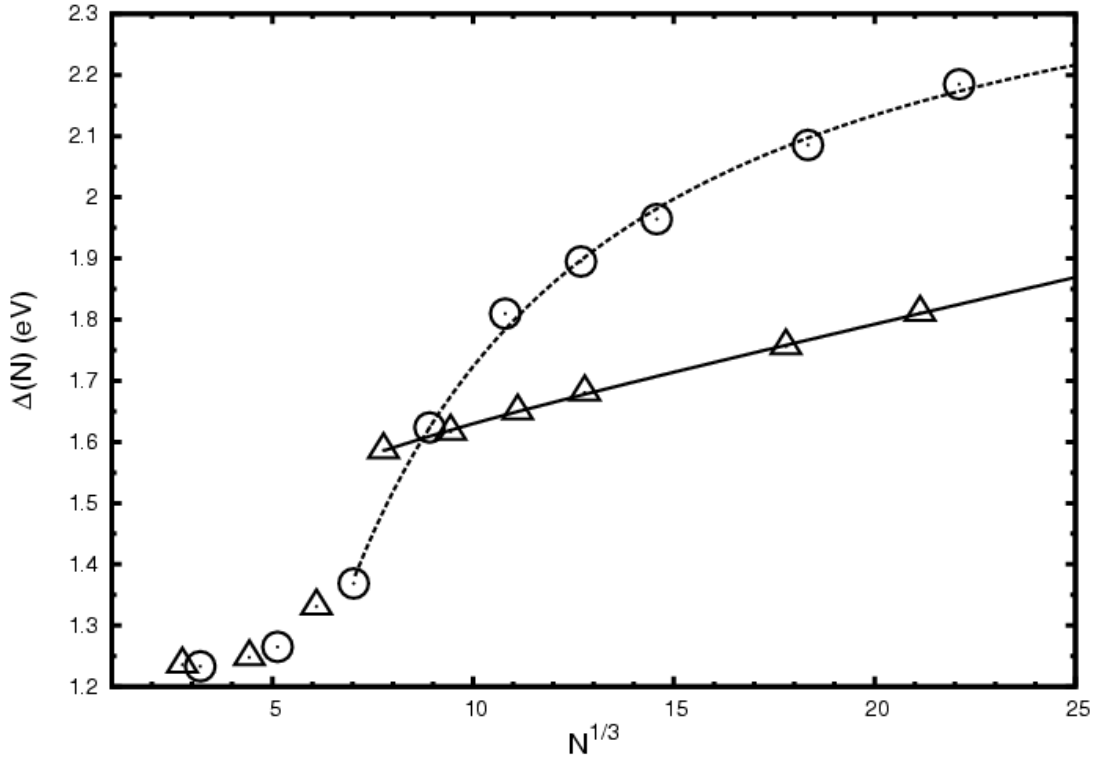


FIG. 9: Same as Fig. (6), but for the MDS results obtained using the CR potential model<sup>19</sup>; the excess energy  $\Delta(N)$  has been calculated using the total energy. Note that we have excluded from the fitting the smallest clusters, since they are low-symmetry or amorphous structures with non star-like shape.

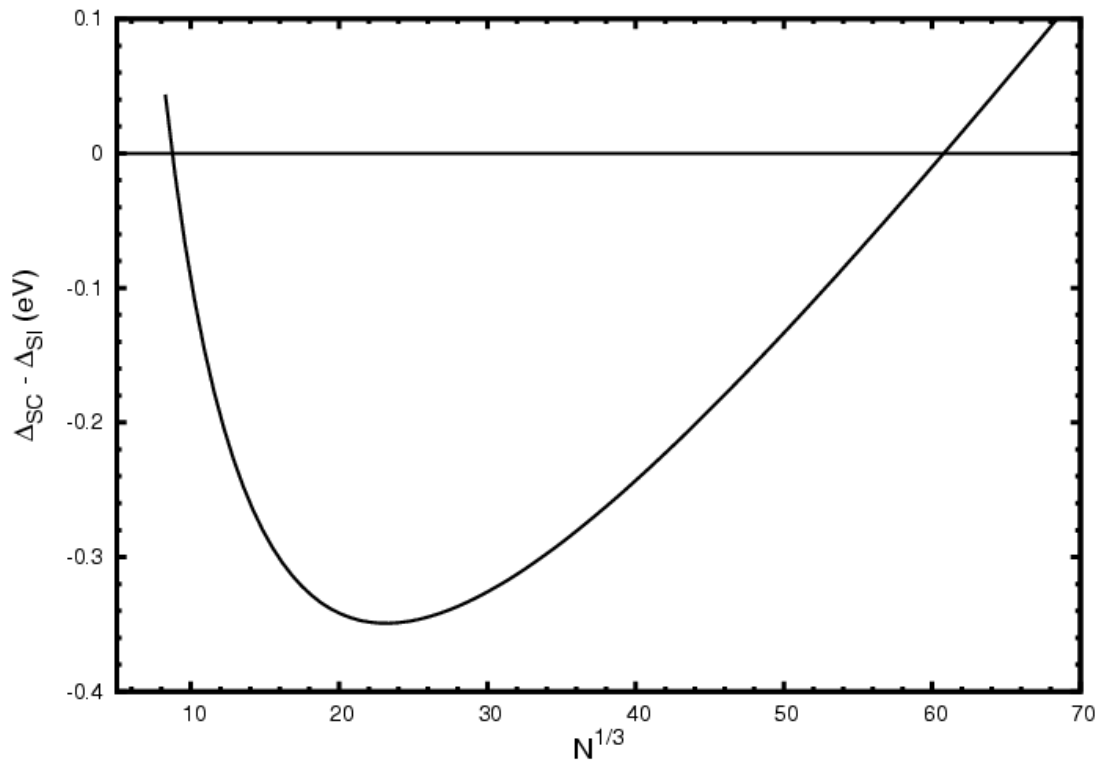


FIG. 10: The difference in excess energy or binding energy per  $N^{2/3}$  of the SC and SI clusters as function of cluster size. The curve is obtained from the fitted curves in Fig. 8.

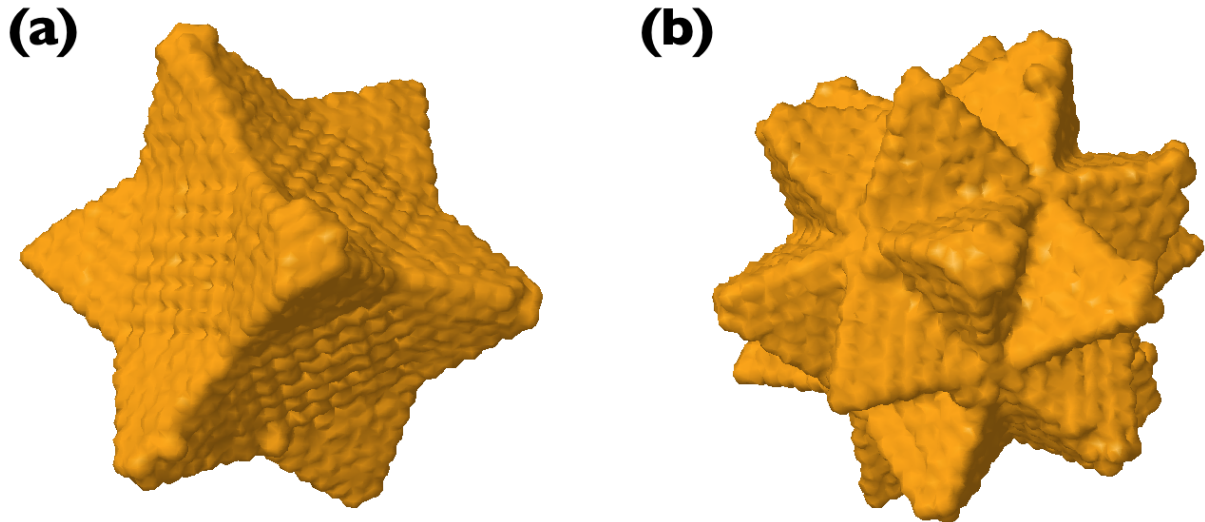


FIG. 11: Snapshots of the equilibrated stellated cuboctahedral and icosahedral clusters. In (a) the clusters has  $N_{\text{SC}}(12) = 9437$  atoms at  $T = 298 \pm 0.46$  K. The diameter of the cluster is around 10.8 nm; in (b) the cluster has  $N_{\text{SI}}(11) = 10803$  atoms. In this case  $T = 298 \pm 0.44$  K, and the diameter of the cluster is around 10.0 nm. To enhance surface details a molecular surface representation computed through the Lee-Richard algorithm<sup>35</sup> has been used.